# Flow-tube Oxidation Experiments on the Carbon Preform of PICA

Francesco Panerai[1] and Alexandre Martin[2]
*University of Kentucky, Lexington, KY, USA 40506-0503*

Nagi N. Mansour[3]
*NASA Ames Research Center, Moffett Field, CA, USA 94035*

Steven A. Sepka[4]
*ERC, Incorporated, Huntsville, AL, USA 35805*

Jean Lachaud[5]
*University of California Santa Cruz, Moffett Field, CA, USA 94035*

**Oxidation experiments on the carbon preform of a phenolic-impregnated carbon ablator were performed in a flow-tube reactor facility, at temperatures between 700 and 1300 K, under dry air gas at pressures between $1.6\times10^3$ and $6.0\times10^4$ Pa. Mass loss, volumetric recession and density changes were measured at different test conditions. An analysis of the diffusion/reaction competition within the porous material, based on the Thiele number, allows to identify low temperature and low pressure conditions to be dominated by in-depth volume oxidation. Experiments above 1000 K were found at transition conditions, where diffusion and reaction occur at similar scales.**

**The microscopic oxidation behavior of the fibers was characterized by scanning electron microscopy and energy dispersive x-ray analysis. The material was found to oxidize at specific sites forming a pitting pattern distributed over the surface of the**

---

[1] Postdoctoral Scholar, Department of Mechanical Engineering, 151 Ralph G. Anderson Building. Visiting Scientist, Thermal Protection Materials Branch, Mail Stop 234-1, NASA Ames Research Center, Moffett Field, CA, 94035, AIAA Senior Member.
[2] Assistant Professor, Department of Mechanical Engineering, Associate Faculty at the Center for Computational Science, 261 Ralph G. Anderson Building, AIAA Senior Member.
[3] Chief Scientist, Advanced Supercomputing Division, Mail Stop 258-1, AIAA Associate Fellow.
[4] Senior Research Scientist, Thermal Protection Materials and Systems Branch, NASA Ames Research Center, Moffett Field, CA, 94035, AIAA Member.
[5] Scientist, Silicon Valley Initiatives, NASA Ames Research Park, Building 19, AIAA Senior Member.

**fibers. Calcium- and oxygen-rich residues from the oxidation reactions were observed at several locations.**

**Nomenclature**

$A$ = pre-exponential factor, m/s

$D$ = tube diameter, m

$\mathcal{D}$ = diffusion coefficient, $m^2/s$

$\mathscr{D}$ = binary diffusion coefficient, $m^2/s$

Da = Damköhler number

$d$ = fiber or pore diameter, m

$E$ = Energy, J/mol

$G$ = Gibbs free energy, J/mol

$k$ = reactivity, m/s

$k_B$ = Boltzmann constant, $1.3806488\times10^{-23}$ J/K

$L$ = characteristic length, m

$l$ = length, m

$m$ = mass (also atomic or molecular mass), kg

$\dot{m}$ = mass flow, kg/s

$n$ = number density, $m^{-3}$

$p$ = pressure, Pa

$\bar{Q}$ = cross-section, $m^2$

$R$ = ideal gas constant, 8.314 J/(mol·K)

Re = Reynolds number

$s$ = specific surface, $m^2/m^3$

$T$ = temperature, K

$u$ = axial velocity, m/s

$V$ = volume, $m^3$

$\bar{v}$ = mean molecular velocity (agitation), m/s

$w$ = wall thickness, m

$x, y, z, t$ = space (m) and time (s) coordinates

$x$ = mole fraction

$\delta$ = thickness, m

$\Delta$ = variation

$\eta$ = tortuosity

$\varepsilon$ = porosity

$\Phi$ = Thiele number

$\rho$ = density, $kg/m^3$

$\bar{\lambda}$ = mean free path, m

$\mu$ = dynamic viscosity, mP

*Superscripts*

0 = standard

$(1,1)$ = diffusion

*Subscripts*

$a$ = activation

$b$ = bulk

$e$ = entrance

eff = effective

$f$ = fiber

$f$ = final

$g$ = gas

$i, j$ = relative to species "i" or "j"

$K$ = Knudsen

$p$ = pore

$r$ = reaction

ref = reference

$s$ = surface

0 = initial

## I. Introduction

The entry of a spacecraft into a planetary atmosphere in a high enthalpy thermo-chemical environment requires a suitable heat shield to protect the spacecraft and its payload from the surrounding high temperature gas. For moderate speed entry, typically below 7.5 km/s, and mild heat fluxes, up to 1 MW/m$^2$, reusable materials are an adequate solution. A famed example are the ceramic tiles of the Space Shuttle orbiter. Entry speeds higher than 8 km/s, heat fluxes exceeding 1.5 MW/m$^2$, and entry into high density atmospheres impose the use of ablative thermal protection systems. These mitigate the incoming heating through phase changes, chemical reactions and material removal. The last decade has seen a renewed effort by scientists and engineers towards the development of a new class of low density carbon/resin ablators, made of a carbon fiber preform impregnated in phenolic resin. A successful example is the phenolic-impregnated carbon ablator (PICA) developed at NASA Ames Research Center and flight qualified during the recent reentry missions of Stardust (Earth reentry at 12 km/s) and Mars Science Laboratory (Mars entry at 5.5 km/s). SpaceX has also successfully flown this class of ablators as heatshield for a commercial return capsule.

One of the remarkable attributes of carbon/phenolic ablators is their versatility. For instance, different carbon preforms could be used to adapt the properties of the impregnating matrix to the characteristics of the flight trajectory. Despite a high technology readiness level, large design margins are applied during TPS sizing due to the numerous assumptions needed on material properties and their physical response, at the expense of mass budget and cost. To help quantify design uncertainties, state of the art pyrolysis-ablation models [1–6] are being revisited. These models, proven as reliable engineering tools by recent missions, still showed significant discrepancies with

flight data [7, 8]. A multi-scale approach has been proposed by Lachaud *et al.* [9, 10] in order to improve understanding of the behavior of carbon/phenolic composites. One of the new features, not available in state-of-the-art tools, is a microscopic scale volume-averaging model for the oxidation of carbon fibers and charred phenolic-polymer matrix. Despite numerous high enthalpy wind tunnel tests [11] and flight data available [12] in the literature, dedicated testing and quantification of the different parameters and material properties is needed to validate this model.

The effort under which the experimental results presented in this paper take place aims at performing fundamental experiments that can decouple, and therefore separately address the various effects occurring during the ablation process of a carbon/phenolic composite. In particular, this paper documents oxidation experiments on the carbon preform of PICA in the NASA Ames flow-tube reactor.

The choice of testing the carbon preform alone allows us to separately address and accurately characterize oxidation properties of the fibers. For example, this prevents complications to the problem that would arise from the simultaneous pyrolysis of phenolic resin in phenolic-impregnated ablators. Additionally, there are practical applications to the analysis of the sole carbon preform. Post-fight evaluations [12] and theoretical analyses [9] showed that, for this class of ablators, in-depth reactions occur, leading to the removal of the more reactive phenolic matrix and leaving the carbon fiber unprotected, hence directly exposed to reactions with the incoming flow. Data on carbon preform alone are also of interest when exploring versions of very low-density carbon/phenolic ablators based on small quantities of phenolic polymer or on non-impregnated carbon preforms.

A first validation effort performed in a tubular reactor addressed the oxidation of carbon preform in air at ≈900 K [13]. It demonstrated the capability of the model to predict surface recession and oxidation penetration. It was decided to continue the study and extend the temperature and pressure ranges of this experiment. The material is tested under dry air at pressures from 1.6 to 60 kPa and temperatures from 700 to 1300 K, promoting the recession of the carbon fibers by oxidation reactions. As shown in Fig. 1, the leading chemical process is the oxidation of solid C into $CO_2$ ($C_{(s)} + O_2 \longrightarrow CO_2$) for $T$ below 973 K and into CO at higher temperatures ($C_{(s)} + \frac{1}{2}\, O_2 \longrightarrow CO$), where carbon monoxide production is thermodynamically more favorable ($\Delta G^0$ is smaller). In excess

of $CO_2$ a third reaction, $C_{(s)} + CO_2 \longrightarrow 2\,CO$, may also occur. $CO_2$ is thus transformed into CO by carbon oxidation when going to the higher temperature region, and CO is transformed into $CO_2$ going in the lower temperature region. It is important to note that in the latter case, solid carbon is formed through this process. The reversible reaction $2\,CO \longleftrightarrow CO_2 + C_{(s)}$ is called the Boudouard reaction, and the conversion occurring at 973 K is known as the Boudouard's equilibrium.

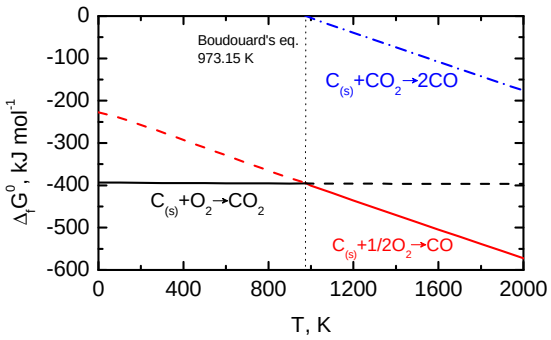


**Fig. 1 Ellingham diagram [14] for carbon oxidation. Gibbs free energy data are taken from NIST-JANAF tables [15]. Below the Boudouard equilibrium at 973 K the leading reaction is the oxidation C into $CO_2$, above 973 K Gibbs free energy favors the production of CO.**

The mass loss and recession of hollow cylindrical (short pipe) specimens are characterized, using macroscopic and microscopic techniques. The paper intends to document a complete set of experiments and their analysis using state-of-the-art techniques.

## II. Experiment

Experiments are performed in the NASA Ames flow-tube reactor shown in Fig. 2. The facility consists of a quartz main tube, connected to a right angle 2.5 cm diameter side arm, where the test section is located. High purity air (Ultra Zero Grade 99.999%, Matheson Tri-Gas®, San Jose, CA, United States) and helium (Ultra High Purity Grade 99.999%, Matheson Tri-Gas®, San Jose, CA, United States) are supplied into the reactor, upstream of the tubes intersection, and regulated using metering valves and calibrated mass flow meters (FM-360, Tylan Corp., Torrance, CA, United States). To operate the facility as a flow-tube the main arm is sealed downstream the intersection by a Teflon® valve, kept closed throughout the test. The system is evacuated using a mechanical pump, connected right before the dead-end of the side-arm. The pressure is monitored using two

capacitance manometer gauges (622B Baratron®, MKS Instruments, Andover, MA, United States), operating in 1 torr and 1000 torr ranges respectively, and regulated by a PID controller of the outlet section throttle valve. The central part of the quartz side-arm is enclosed in a clam-shell electric furnace, spanning a region of approximately 470 mm, and providing temperatures up to 1500 K. The furnace covers a length large enough to ensure that both the sample and the gas are heated to the target temperature. Prior to testing, the specimen is placed at the middle section of the furnace using glass holders and extension tubes.

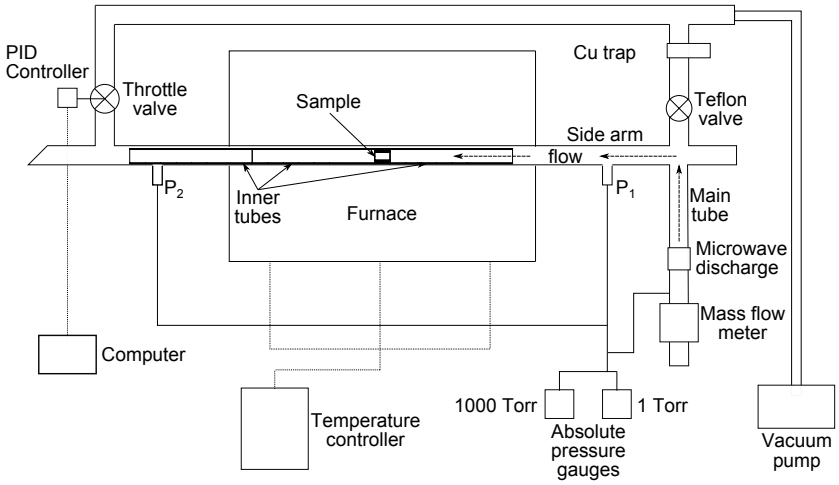


**Fig. 2 Schematic of the NASA Ames flow-tube test setup.**

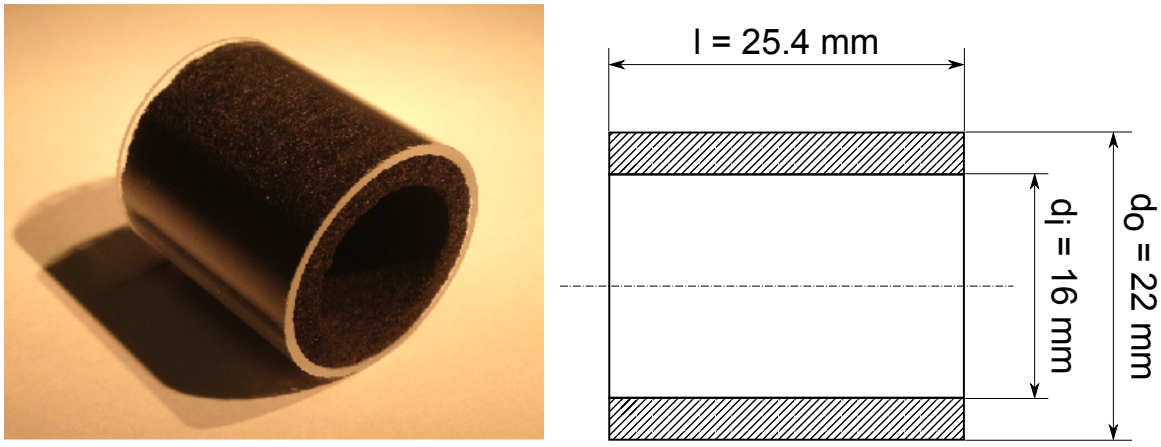


**Fig. 3 Hollow cylinder carbon preform sample. The top picture shows the specimen fit into the glass holder, on the bottom sketch of the specimen geometry is detailed.**

The material studied in this paper is FiberForm,® an industrial carbon preform manufactured

by Fiber Material Inc. (Biddeford, ME, United States). It is developed for industrial thermal furnaces insulation and is selected by NASA as precursor for PICA. Sample geometry for the experiments reported, shown in Fig. 3, is a 25.4 mm height hollow cylinder, with 16 mm internal diameter and 22 mm external diameter. The specimen is interference-fit into a glass holder placed at the middle section of the heating furnace. Three 220 mm long glass tubes are placed, with contact, one upstream of the sample holder and two downstream, in order to avoid facing steps and ensure a fully developed pipe flow.

The test procedure consisted in sealing the tubes, evacuating the system to a base pressure below 10 Pa and feeding it with a low helium flow (below 0.03 mg $s^{-1}$) while the furnace is heating up to the target temperature condition. The supply of He ensured that no oxidation reaction occurred during the transient heating phase. Once the temperature is stabilized, the He flow is stopped, the chamber is evacuated again down to 100 Pa, and dry air flow is started at the desired rate. The test gas supply caused the pressure to rise to the target value, where the regulation is taken over by the PID controller, by adjusting the suction rate of the mechanical pump downstream the samples. The transient phase to the target pressure is monitored to have a duration of $\approx$1 min for the lowest pressure condition (1.6 kPa) and $\approx$5 min for the highest value (60 kPa). Mass flow and pressure are maintained constant throughout the test time. The experiment ended with a final evacuation of the test section below 100 Pa and a restoring of the He flow, during the cooling phase of the system.

The test conditions are detailed in Table 1. The experiments are performed at temperatures from 700 to 1300 K, using steps of 100 K, and pressures of 1.6, 10 and 60 kPa, maintained for a total of 1 hour of oxidation time during each run. Gas properties are calculated using the Chemical Equilibrium with Applications (CEA) code [16] from NASA Glenn Research Center. The Reynolds number $\mathrm{Re} = \rho u D/\mu$, based on the 22 mm tube diameter, is below 3.7 at all test conditions, clearly indicating a laminar flow. The calculated Re confirms also that the flow is fully developed at the sample's location. For a laminar flow in a pipe of diameter $D$, the entrance length $L_e$ can be estimated from the relation $L_e/D = 0.06\,\mathrm{Re}$. For the present setup $L_e \lesssim 6$ mm, well below the 220 mm of the upstream extension tube.

The three pressure levels are selected to cover three different transport conditions within the

porous material, as shown in Figure 4. The plot, proposed in Ref. [9], presents Knudsen number (mean free path $\bar{\lambda}$ to mean pore diameter $d_p$ ratio) regimes from continuum to rarefied, calculated for a mean pore diameter of 50 µm for carbon preform. Experiments at 1.6, 10 and 60 kPa cover respectively continuum, slip and transition regimes within the pores of the material. The Stardust trajectory is shown as reference on the same graph to highlight that the flow regime at the fiber scale is different than the regime at the capsule scale (typically continuum during the portion of reentry where ablation is relevant [17]). The characteristic scale of the porous medium (the pore diameter) is much smaller than that of the TPS body, hence the dynamics of oxidant transport at micro-scale is different from the incoming gas regime.

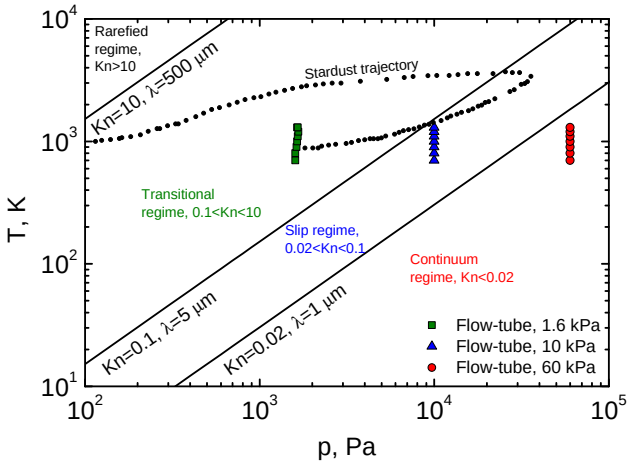


**Fig. 4 Flow-tube regimes compared to the Stardust trajectory.**

Different techniques are applied to analyze the carbon preform prior to and post flow-tube oxidation. Mass measurements are performed using an analytical balance (AB104S, Mettler-Toledo, LLC, Columbus, OH, United States) with ±0.1 mg accuracy. A caliper is used to document changes in length, inner diameter and outer diameter with ±0.1 mm precision. The bulk density of the material is estimated as the ratio between the mass measured with the balance and the volume calculated from caliper measurements. Initial densities of the specimens are calculated between 165 and 185 kg $m^{-3}$, with an uncertainty of ±6 kg $m^{-3}$. Density changes for all the specimens are documented in Section III.

In order to determine the exact volume recession due to oxidation for each sample, a suitable

**Table 1 Summary of flow tube test conditions: pressure, temperature, oxidation time, mass flow rate, velocity, gas density, gas viscosity and Reynolds number**

| Sample # | $p$, kPa | $T$, K | $t$, min | $\dot{m}$, mg s$^{-1}$ | $u$, m s$^{-1}$ | $\rho_g$, kg m$^{-3}$ | $\mu_g$, mP | Re |
|---|---|---|---|---|---|---|---|---|
| a1 | 1.60 | 700 | 60 | 2.18 | 0.719 | 0.00796 | 0.34288 | 3.67 |
| a2 | 1.60 | 800 | 60 | 2.19 | 0.827 | 0.00697 | 0.37563 | 3.38 |
| a3 | 1.63 | 900 | 60 | 2.19 | 0.930 | 0.00619 | 0.40688 | 3.12 |
| a4 | 1.64 | 1000 | 60 | 2.19 | 1.034 | 0.00557 | 0.43688 | 2.90 |
| a5 | 1.63 | 1100 | 60 | 2.21 | 1.145 | 0.00507 | 0.46572 | 2.74 |
| a6 | 1.64 | 1200 | 60 | 2.21 | 1.249 | 0.00464 | 0.49355 | 2.59 |
| a7 | 1.64 | 1300 | 60 | 2.18 | 1.335 | 0.00429 | 0.52059 | 2.42 |
| b1 | 10 | 700 | 60 | 2.19 | 0.116 | 0.04977 | 0.34288 | 3.70 |
| b2 | 10 | 800 | 60 | 2.19 | 0.132 | 0.04355 | 0.37563 | 3.38 |
| b3 | 10 | 900 | 60 | 2.19 | 0.149 | 0.03871 | 0.40688 | 3.12 |
| b4 | 10 | 1000 | 60 | 2.18 | 0.164 | 0.03484 | 0.43688 | 2.88 |
| b5 | 10 | 1100 | 60 | 2.19 | 0.182 | 0.03167 | 0.46572 | 2.72 |
| b6 | 10 | 1200 | 60 | 2.21 | 0.200 | 0.02903 | 0.49355 | 2.59 |
| b7 | 10 | 1300 | 60 | 2.18 | 0.214 | 0.02680 | 0.52059 | 2.42 |
| c1 | 60 | 700 | 60 | 2.19 | 0.019 | 0.29860 | 0.34288 | 3.70 |
| c2 | 60 | 800 | 60 | 2.19 | 0.022 | 0.26128 | 0.37563 | 3.38 |
| c3 | 60 | 900 | 60 | 2.19 | 0.025 | 0.23225 | 0.40688 | 3.12 |
| c4 | 60 | 1000 | 60 | 2.19 | 0.028 | 0.20902 | 0.43688 | 2.90 |
| c5 | 60 | 1100 | 60 | 2.21 | 0.031 | 0.19002 | 0.46572 | 2.74 |
| c6 | 60 | 1200 | 60 | 2.21 | 0.033 | 0.17418 | 0.49355 | 2.59 |
| c7 | 60 | 1300 | 60 | 2.21 | 0.036 | 0.16079 | 0.52059 | 2.45 |

post test method is implemented to cope with the brittleness of the carbon preform specimens. The oxidized samples are found to easily crumble into pieces in any attempt of manual extraction from the glass holder. Therefore, the specimen/holder assembly is impregnated in epoxy resin, by means of an encapsulation chamber (Epovac, Struers A/S, Ballerup, Denmark) capable of 100 mbar terminal vacuum. A resin/hardener mixture (CaldoFix, Struers A/S, Ballerup, Denmark) is poured into a plastic mold hosting the assembly and oven-cured for 2 hours ≈343 K. The encapsulated

specimen is then sectioned along axial symmetry plane using a diamond wheel cut-off machine (Accutom-50, Struers A/S, Ballerup, Denmark).

Pictures of the specimen are acquired using a commercial reflex camera, and the area of interest is filtered using Fiji [18] and digitized using Enguage [19], in order to extract the oxidation profiles coordinates (see Fig. 5). The actual volume loss (recession) is computed by integration the extracted profiles.

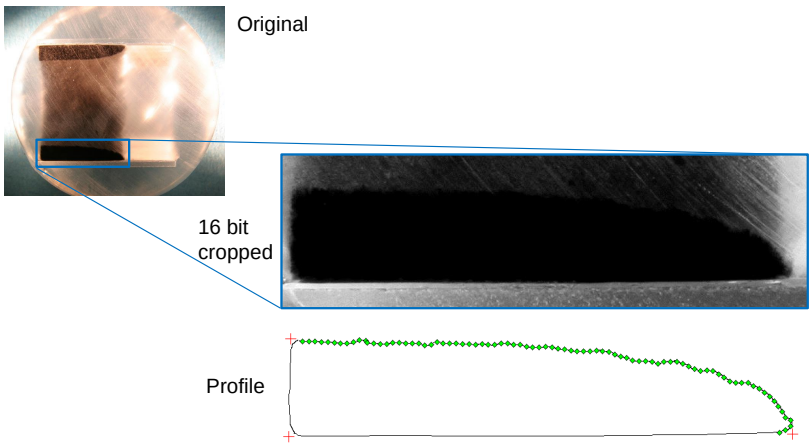


**Fig. 5 Elaboration of optical microscope images.**

An environmental scanning electron microscope (XL30 ESEM, FEI, Hillsboro, OR, United States) is used to characterize the morphology of the fiber prior to and post oxidation tests. Energy dispersive x-ray spectrometry (EDX) allowed analyzing the specimens chemical composition.

## III. Results

Micrographs of the virgin material are shown in Fig. 6. During manufacturing, Fiberform's fibers are bonded together with a phenolic resin, that is fully carbonized through high temperature processing. Carbon bonds between the fibers can be seen at the fibers intersections in the SEM images of Fig. 6. Fibers are found to have an average diameter $d_f$ between 9 and 13 µm and an average length $l_f$ between 100 and 500 µm. Bundles or clusters, where multiple fibers are bounded, are observed at several locations throughout the sample. Similar structures are documented for an analogous rayon-based preform material (Calcarb®) [20], used to produce European lightweight ablators as well as SpaceX's replica of PICA, PICA-X.

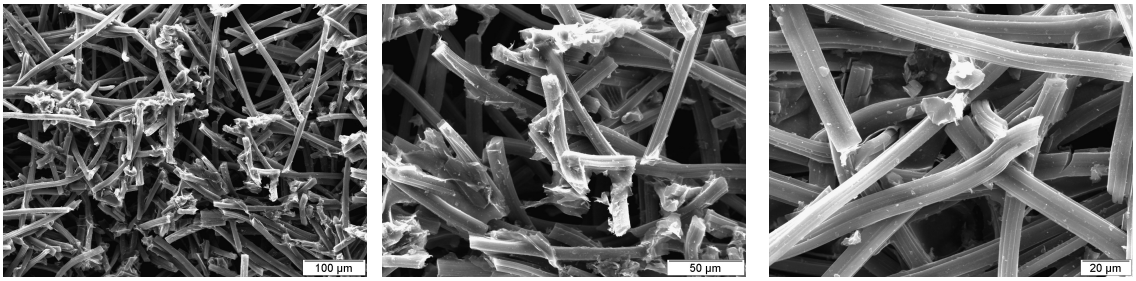


**Fig. 6 Scanning electron micrographs of virgin carbon preform at different magnification levels.**

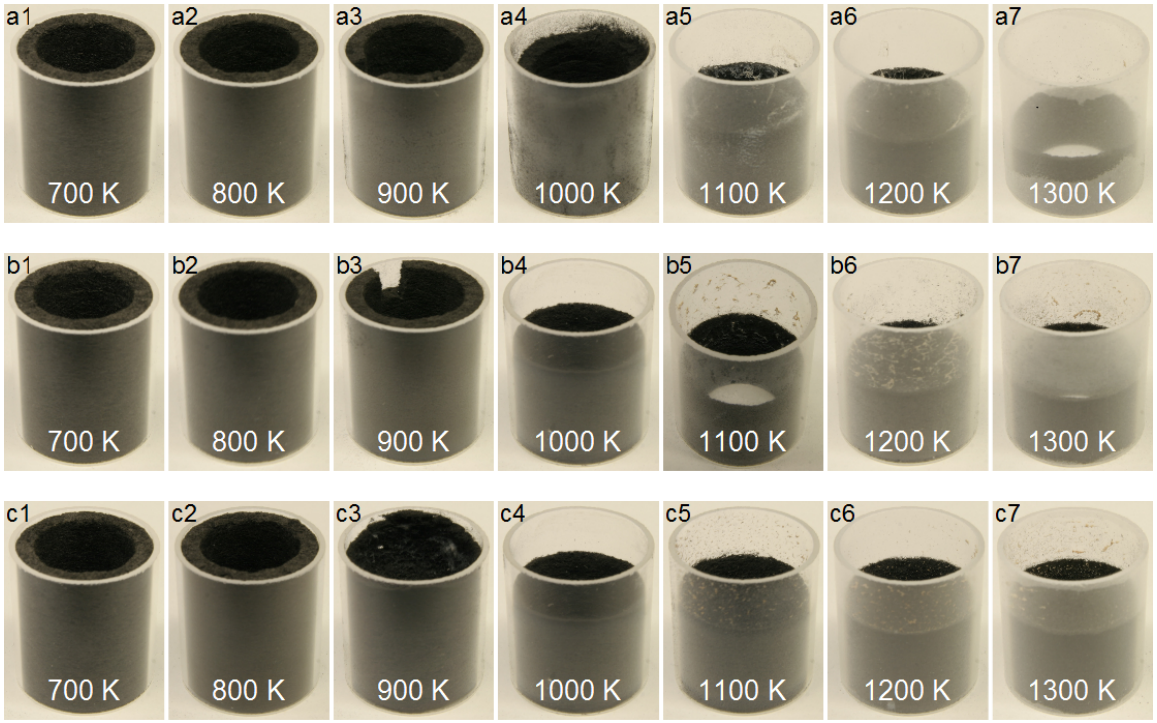


**Fig. 7 Post test pictures of carbon preform samples in the glass holder. Top row to bottom: specimens tested at 1.6 kPa, 10 and 60 kPa. The small pieces that are missing on specimens a3 and b3 are extracted for analysis before the pictures are taken.**

Carbon preform samples, tested in low pressure dry air for 1 hour, are subjected to ablation by oxidation. The correspondent material loss depends on the temperature to which the specimens are exposed.

Several features can be observed looking at the specimens after the experiments (see Figs. 7, 8 and 9). No visible recession can be observed at temperatures below 900 K. Nevertheless, while the material keeps its integrity and strength at the lowest temperatures (700 and 800 K), specimens at

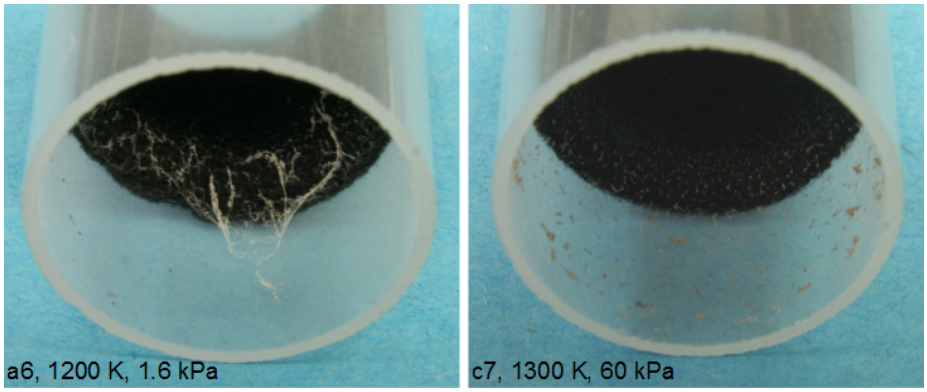


**Fig. 8 Highlight of impurities depositions on the glass holder walls.**

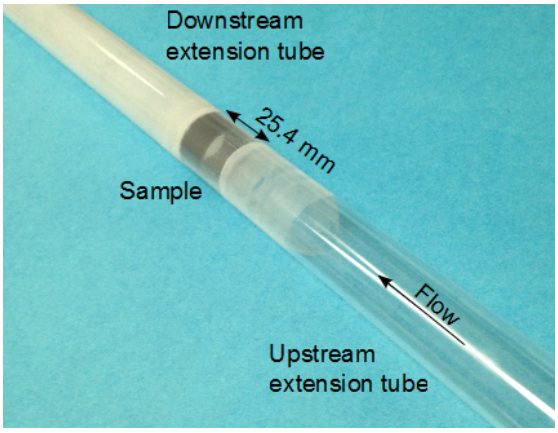


**Fig. 9 Upstream and downstream extension tubes. Impurities' deposition is also visible on the walls of both tubes; the upstream deposition is caused by diffusion of the outgassing ablation products.**

900 K are found to be very brittle, a soft touch being sufficient to crumble the material at the front surface (the one exposed to the flow). Samples a4 and c3 in Fig. 7 showed the material in early phases of surface recession with top fibers nearly completely eroded by oxygen attack.

Leftover depositions on the glass walls are observed for specimens tested at 1100 K temperature and above, with different consistency and structure depending on the pressure. Examples are shown in Fig. 8. Depositions at 1.6 kPa present a whitish color and spider's web-like filamentous structure, easily removable with a gentle blowing action, while specimens at 10 and 60 kPa show brownish, harder structures, stuck to the glass walls. EDX analyses show that these are calcium- and oxygen-rich residues, with traces of other species like silicon, sodium, sulfur and potassium. Similar

compositions are observed over oxidized carbon fibers at several locations on tested samples, as shown in Fig. 10. Reference [13] reported that the presence of Ca and O traces, found by EDX, suggests oxidation residues to be calcium carbonate ($CaCO_3$). The impurities are believed to act as catalysts for oxidation reactions, providing higher reactivities than those typically reported in the literature [13, 21].

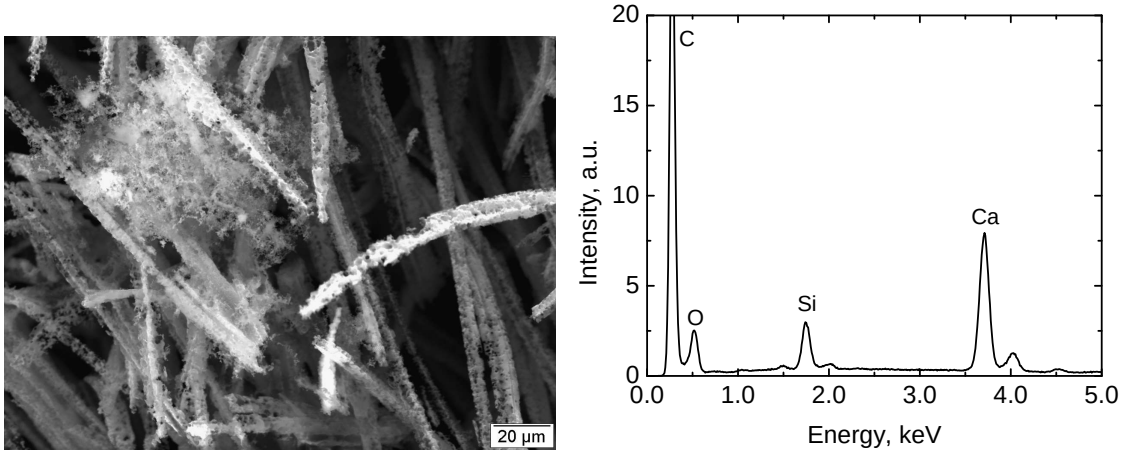


**Fig. 10 SEM micrograph (left) and EDX analysis (right) of oxidation residues.**

Figure 9 shows a post test picture of the extension glass tubes that provide continuity with the sample. One can notice that the downstream portion is completely covered by a whitish opaque scale, likely to be caused by deposition of combustion residues on the walls. Attempts undertaken to clean the tubes return little success: the residues are tenaciously calcified to the glass walls. Interestingly, the same residue deposition is observed on the tube in front of the sample, up to almost 5 cm upstream of the specimen. A CFD analysis of this configuration ruled out any possibility of a recirculation zone in front of the sample, which therefore suggest that this residue is caused by the upstream diffusion of outgassing products. This residue could be used as a rough indicator on how far the ablation products, like $CO_2$, diffuse in front of the sample.

Table 2 lists changes in mass, volume and density of carbon preform samples measured prior to and post flow-tube testing. The volume of the virgin material is calculated from caliper measurements of inner diameter, outer diameter and length assuming an ideal (hollow) cylindrical shape. Post test value are calculated by integrating the digitized profiles extracted from encapsulated sam-

**Table 2 Mass, volume and density values of carbon preform prior to (subscript 0) and post (subscript $f$) oxidation**

| Sample # | $p$, kPa | $T$, K | $m_0$, g | $m_f$, g | $V_0$, mm$^3$ | $V_f$, mm$^3$ | $\rho_0$, kg m$^{-3}$ | $\rho_f$, kg m$^{-3}$ |
|---|---|---|---|---|---|---|---|---|
| a1 | 1.60 | 700 | 0.781 | 0.759 | 4424 | 4349 | 176.5 | 174.6 |
| a2 | 1.60 | 800 | 0.762 | 0.455 | 4436 | 4010 | 171.8 | 113.5 |
| a3 | 1.63 | 900 | 0.765 | 0.448 | 4479 | 3629 | 170.9 | 123.4 |
| a4 | 1.64 | 1000 | 0.754 | 0.343 | 4509 | 3193 | 167.3 | 107.4 |
| a5 | 1.63 | 1100 | 0.749 | 0.297 | 4439 | 2154 | 168.8 | 137.7 |
| a6 | 1.64 | 1200 | 0.752 | 0.267 | 4500 | 1852 | 167.2 | 144.1 |
| a7 | 1.64 | 1300 | 0.773 | 0.184 | 4568 | 1337 | 169.1 | 137.7 |
| b1 | 10 | 700 | 0.749 | 0.721 | 4350 | 4312 | 172.2 | 167.2 |
| b2 | 10 | 800 | 0.755 | 0.502 | 4556 | 3972 | 165.6 | 126.3 |
| b3 | 10 | 900 | 0.766 | 0.420 | 4389 | 3890 | 174.5 | 108.1 |
| b4 | 10 | 1000 | 0.760 | 0.356 | 4391 | 2545 | 173.1 | 139.7 |
| b5 | 10 | 1100 | 0.732 | 0.318 | 4440 | 2001 | 164.8 | 158.7 |
| b6 | 10 | 1200 | 0.733 | 0.287 | 4381 | 1751 | 167.3 | 163.7 |
| b7 | 10 | 1300 | 0.838 | 0.256 | 4522 | 1788 | 185.4 | 143.2 |
| c1 | 60 | 700 | 0.756 | 0.705 | 4383 | 4378 | 172.5 | 161.1 |
| c2 | 60 | 800 | 0.750 | 0.450 | 4323 | 3969 | 173.4 | 113.5 |
| c3 | 60 | 900 | 0.745 | 0.381 | 4446 | 2944 | 167.7 | 129.3 |
| c4 | 60 | 1000 | 0.773 | 0.404 | 4405 | 2302 | 175.5 | 175.3 |
| c5 | 60 | 1100 | 0.752 | 0.382 | 4347 | 2240 | 173.0 | 170.6 |
| c6 | 60 | 1200 | 0.754 | 0.363 | 4400 | 2247 | 171.4 | 161.4 |
| c7 | 60 | 1300 | 0.744 | 0.245 | 4419 | 2202 | 168.3 | 111.0 |

ples, shown in Fig. 11. The profiles illustrate the actual shape of the samples after one hour of oxidation at the specified conditions.

Percent mass loss and recession are plotted in Fig. 12. As expected, the general trend of an increasing mass loss with increasing temperature is observed. The $\Delta m/m_0$ rate slows at temperatures higher that 900 K, reaching a plateau around 1200 K, and increases again beyond 1300 K. This behavior is most pronounced at the highest pressure level. For temperatures higher than 900

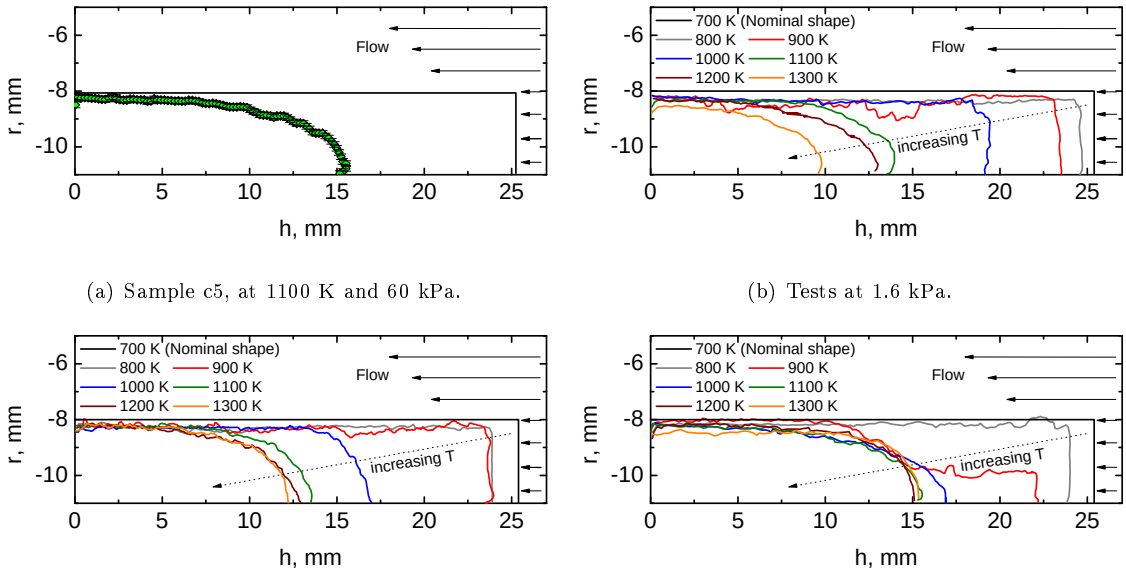


(a) Sample c5, at 1100 K and 60 kPa.

(b) Tests at 1.6 kPa.

(c) Tests at 10 kPa.

(d) Tests at 60 kPa.

**Fig. 11 Digitized oxidized surface profiles of ablated carbon preform samples. Plot (a) shows the profile on Fig. 5 with the associated error bars, documenting the degree of accuracy that can be obtained with the present procedure. Axial and radial axes are not in scale.**

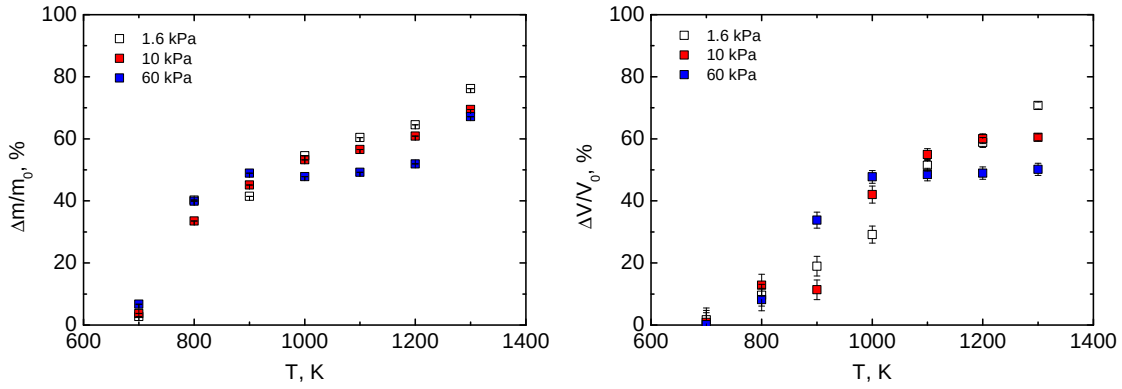


**Fig. 12 Mass (left) and volume (right) loss as a function of surface temperature.**

K, a slight increase in mass loss with decreasing pressure can be noticed.

Although, as mentioned, no recession is observed for specimens tested at temperature from 700 to 900 K by measuring their length, a non-negligible volume loss could be calculated by integrating the oxidized surface profiles. To further assess this, it is worth to first analyze the competition between oxidation reactions and diffusional transport at the flow-tube conditions. The dimensionless parameter that is used to characterize such effects for porous materials is the Thiele number, defined

as

$$\Phi = \frac{L}{\left[\mathcal{D}_{\text{eff}}/(s_f k_f)\right]^{1/2}} \tag{1}$$

where $L$ is a characteristic length of the model, $\mathcal{D}_{\text{eff}}$ is the effective diffusion coefficient, $s_f$ is the specific surface of the porous medium and $k_f$ is the fiber reactivity. At high Thiele numbers, ablation is mostly a surface phenomenon, since it is limited by a slow diffusional transport. Conversely, when diffusion is high enough to feed a large flux of reactants for chemical reactions and the reactivity is relatively slow, then the depths of the ablation zone becomes larger (typically larger than the fiber scale) and volumetric ablation is promoted.

In this work, the sample wall thickness $w$ is used as reference length ($L = w = 3$ mm). The effective diffusion coefficient $\mathcal{D}_{\text{eff}}$ for an isotropic porous medium, is given by $\mathcal{D}_{\text{eff}} = \varepsilon\mathcal{D}_{\text{ref}}/\eta$ where $\varepsilon$ is the porosity, $\eta$ the tortuosity and $\mathcal{D}_{\text{ref}}$ the reference diffusivity. The porosity of Fiberform is estimated to be 0.9 by means of micro-tomography measurements [22]. To calculate the reference diffusivity, one should account for the orthotropy of the material: during the manufacturing process of Fiberform, the fibers tend to align parallel to the direction of the pressing plane [23], yielding different $\mathcal{D}_{\text{ref}}$ in the planar and transverse direction. A rigorous method consists of computing $x$-$y$ and $z$ directional diffusivities using random-walk direct numerical simulations [9]. Since the idea is to only obtain an order of magnitude estimation of $\Phi$, these differences are neglected and Bosanquet's relation [24] is used to express the reference diffusivity as:

$$\mathcal{D}_{\text{ref}}^{-1} = \mathcal{D}_b^{-1} + \mathcal{D}_K^{-1} = (1/3\bar{v}\bar{\lambda})^{-1} + (1/3\bar{v}d_p)^{-1} \tag{2}$$

where $\mathcal{D}_b$ and $\mathcal{D}_K$ are the bulk and Knudsen diffusivity respectively. The mean free path (in meters) is calculated [25] as $\bar{\lambda} = 9.5 \times 10^{-8} \cdot 10^5 T \cdot (298p)^{-1}$, the mean pore diameter for Fiberform is 50 µm [9] and the mean molecular velocity is estimated by kinetic theory as $\bar{v} = \sqrt{8k_B T/(\pi m)}$. The tortuosity $\eta$ depends on the Knudsen number and on the orientation as well. Data can be found in Ref. [9], calculated for a random fibrous medium. For the present calculations of $\mathcal{D}_{\text{ref}}$ an averaged value of the $x$-$y$ and $z$ tortuosities is used.

The specific surface area $s_f$, in the approximation of the fibers as cylinders that reduce in

diameter from $d_{f,0}$ to $d_f$, can be written as:

$$s_f = 4\varepsilon_{f,0}\frac{d_f}{d_{f,0}^2} \tag{3}$$

where $\varepsilon_{f,0}$ is the initial fiber volume fraction. Average measurements from the scanning electron micrographs of virgin and oxidized carbon fibers allows to reasonably assume $d_{f,0}$ ≈11 µm and $d_f$ ≈5 µm.

To complete the calculation of the Thiele number, $k_f$ is needed. The underlying objective behind the experiment presented in the paper is to provide a set of data to extract the fiber reactivity by calibration of a numerical model to the match the measured oxidation profiles. A common approach proposed in the literature for reactivity coefficients is to use an Arrhenius formulation with activation energy $E_a$, that reads

$$k_f = Ae^{-E_a/(RT)} \tag{4}$$

To estimate $\Phi$, an activation energy of $E_a$ ≈120 kJ mol$^{-1}$ and a pre-exponential factor $A = 100$ m s$^{-1}$ is used, as given in Ref. [9], based on previous investigation of carbon fiber-based materials [21, 26–28]. The proposed activation energy is also in agreement with data from Rosner and Allendorf on isotropic graphite [29, 30]. It is acknowledged here that any assumption on $k_f$ values is easily questionable. Indeed, discrepancies up to several order of magnitude can be found among literature data. The reason for these discrepancies are various. For instance, there are several differences in the manufacturing processes and thermal treatments of the materials, different experimental conditions as atmospherics gases, reactants, pressures, diffusion effects and so forth. Therefore, dedicated measurements should be carried out on the very material of interest at meaningful test conditions for its application, any time $k_f$ is needed.

Thiele numbers for the flow-tube test conditions, shown in Fig. 13, suggest that for experiments at the lowest temperature and pressure, a reaction-limited regime prevails. This is in agreement with what is observed in $\Delta m/m_0$ and $\Delta V/V_0$ plots, where, at such condition, mass is lost with minor volume change: diffusion is high enough with respect to reaction to provide in-depth oxidation and limited recession. As pressure and temperature increase, the depth of the oxidation decreases and surface and volume recession tend to equilibrate.

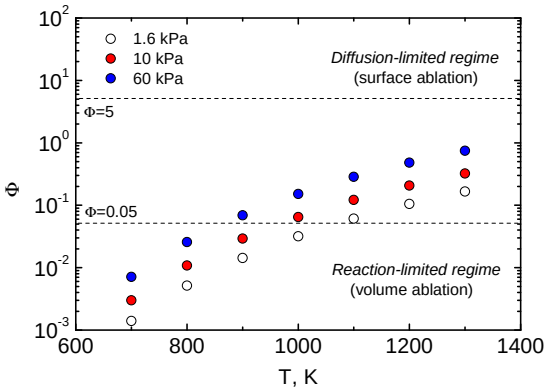


**Fig. 13 Estimated porous medium regime for the flow-tube test conditions.**

In addition to diffusional effects into the porous medium, it is also worthwhile to consider the diffusion/reaction competition at the flow/surface interface. This is described by the Damköhler number:

$$\mathrm{Da} = \frac{\delta_r k_{s,\mathrm{eff}}}{\mathcal{D}} \tag{5}$$

Da compares a surface effective reaction rate $k_{s,\mathrm{eff}}$ to the rate of reactants diffusion to the wall $\mathcal{D}/\delta_r$, where $\delta_r$ is the thickness of the reacting boundary layer. Da is small (<0.01) in reaction-limited regime and high (>100) in diffusion-limited regime.

The maximum possible size of the boundary layer for $\delta_r$ is used (this corresponds to half of the tube diameter, $\delta_r = D/2 = 11$ mm). Numerical simulations of the flow inside the tube will allow to refine this conservative assumption in the future, yet without altering the present conclusions.

For a multi-component mixture, it is possible to compute the average species diffusion coefficients for the species $i$, according to Fick's law, as:

$$\mathcal{D}_i = \frac{1 - x_i}{\sum_{j \neq i} \frac{x_j}{\mathscr{D}_{i,j}}} \tag{6}$$

The binary diffusion coefficients $\mathscr{D}_{i,j}$ are given by:

$$\mathscr{D}_{i,j} = \frac{3}{16} \left( \frac{2\pi k_B T \left(m_i + m_j\right)}{m_i m_j} \right)^{1/2} \frac{1}{n \bar{Q}_{i,j}^{(1,1)}} \tag{7}$$

where $m_i$ and $m_j$ are the atomic (or molecular) mass of the diffusing species $i$ and $j$, and $n = p/(k_B T)$ the number density. The diffusion cross-sections $\bar{Q}_{i,j}^{(1,1)}$ can be obtained from fitting expressions provided by Capitelli et al. [31]. At the present experimental conditions the gas is

not dissociated, only molecular species are present. Using effective reactivities $k_{s,\text{eff}}$ for Fiberform from Ref. [9], Damköhler numbers are calculated to be between $2.7 \times 10^{-5}$ and $8.9 \times 10^{-2}$ for the experiments at 1.6 kPa, between $1.7 \times 10^{-4}$ and $5.5 \times 10^{-1}$ at 10 kPa, and between $1.0 \times 10^{-3}$ and $3.3 \times 10^{0}$ at 60 kPa, increasing with increasing temperature. These values confirm that we are in the reaction-limited regime at all flow conditions in the reactor.

The fiber-scale oxidation of the specimens can be described by the micrographs shown in Fig. 14. These pictures clearly show that mass is lost at localized "active" sites where oxygen molecules react with carbon, resulting in pitting patterns distributed over the fiber surface (see Figs. 14(d) to 14(l)).

In the conditions tested, the complete ablation of a single fiber is caused by an increase of the pitting density over the surface (rather than an increase of the hole size), until the whole fiber surface is covered. A closer analysis of the micrograph reveals that the pit size is $\approx 1 - 2$ µm, roughly of the order of magnitude of $10^6$ carbon atoms. The formation of pits was observed by several authors during previous experiments [32, 33] and simulations [34] on graphite-based materials and discussed in details in [35]. Oxidation reactions mainly occur at the location of a crystalline defect of the pseudo-graphitic structure. The occurrence of an oxidation reaction locally increases the temperature and the size of the crystalline defect. It has been shown that the release of the gaseous oxidation products leaves atomic vacancies (monovacancy defects), that produce an increase in the surrounding atoms' electronic density, leading to an enhancement of the oxidation rate [35–37]. As a result, once activated, the phenomenon propagates from the location of the primary attack over the graphene plane, similar to a self-augmenting reaction. One could picture it as a puddle spreading on the ground. Finally, from the finite size of the pits diameter, it could be inferred that the density of the pits is related to the density of the pseudo-grains composing the crystalline structure. A pit would continue to spread until the whole pseudo-grain is covered. This would also explains why, as observed, the complete decomposition of a fiber does not occur because of the continuous increase of the pits' diameter, but due to an increase in the number of pits.

Interestingly, it can be noticed that despite the randomness of the pitting, the distribution of active oxidation locations is uniform throughout the fiber surface. That is, there is no higher density of holes at a specific region along the fiber length (like, for instance, on the upstream portion of a

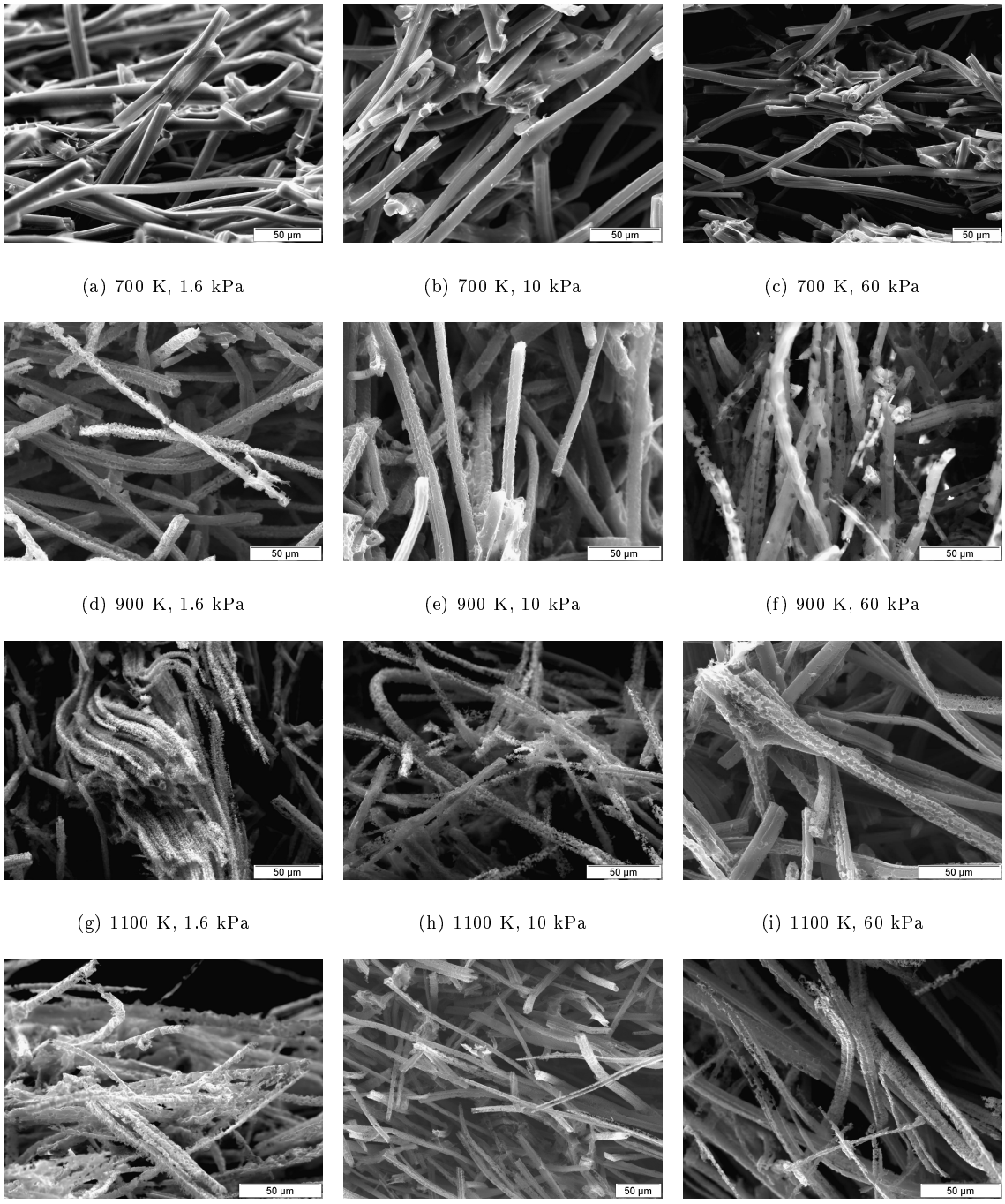


(a) 700 K, 1.6 kPa (b) 700 K, 10 kPa (c) 700 K, 60 kPa

(d) 900 K, 1.6 kPa (e) 900 K, 10 kPa (f) 900 K, 60 kPa

(g) 1100 K, 1.6 kPa (h) 1100 K, 10 kPa (i) 1100 K, 60 kPa

(j) 1300 K, 1.6 kPa (k) 1300 K, 10 kPa (l) 1300 K, 60 kPa

**Fig. 14 Micrographs of oxidized carbon preform at different flow-tube conditions.**

fiber whose aspect ration is oriented in the direction of diffusion of the flow through the pores). As a result, fibers show uniform thinning (i.e. diameter reduction) over the whole fiber length. This is noticed at all temperatures below 1300 K and at the three pressures applied during testing. SEM of specimens tested at the highest temperature showed instead icicle shaped fibers, where the fiber

diameter reduces from the bottom to the top of the fiber. Icicle shaped fibers were observed in carbon preform specimens tested in a high-enthalpy induction plasma torch at temperature above 2000 K [20] and in carbon samples exposed to nearly 3000 K in arc-jet flow [38].

## IV. Conclusion

Data were presented from flow-reactor experiments on carbon fiber preform. Twenty-one hollow cylinder models were tested in the NASA Ames flow-tube reactor facility under laminar dry air, at temperatures from 700 to 1300 K and pressures of 1.6, 10 and 60 kPa. Mass loss and recession data were measured and the change of the material morphology at fiber-scale was characterized using scanning electron microscopy. It was found that the microscopic oxidation of fibers occurs at specific sites where oxygen attacks the carbon, forming a pitting pattern distributed over the surface. The oxidation of the fibers leads to a progressive reduction of their diameter. Both visual observation and microscopic analysis showed the presence of combustion residues in between carbon fibers, that EDX analysis confirmed to be calcium- and oxygen-rich structures.

An order of magnitude estimation of Thiele and Damköhler numbers allowed to assess the diffusion/reaction processes in the porous medium and at the fluid/surface interface. Low pressures ($\leq$ 10 kPa) and low temperatures ($\leq$ 900 K) promote a reaction limited regime in the porous medium, where oxidation is mostly a volumetric process. Thiele number increases as pressure and temperature increase. Most of the experiments are in a transition regime where reaction and diffusion control conditions are balanced. The transport of oxidant to the surface is high enough to prevent any diffusion limitation at the material surface.

This paper provides the necessary data to enable numerical modeling of the flow-tube environment and the recession of carbon preform by oxidation. This will allow to obtain an estimate of the temperature dependent effective fiber reactivity for the material of interest, as well as to improve the calculation of $\Phi$ and Da. Reaction rates to be used for materials response analyses and CFD simulations will be derived from the present measurements and presented in future publications.

## V. Acknowledgements

Financial support to the first author of this work was provided by NASA SBIR Phase-2 Award NNX10CC53P, and NASA Kentucky EPSCoR Award NNX10AV39A. Support by the Hypersonic EDL program for the effort is gratefully acknowledged. We thank the unwavering encouragements by M. J. Wright (NASA Ames Research Center) and A. M. Calomino (NASA Langley Research Center). We are also thankful to J. Chavez Garcia (ERC, Inc.) for the support on scanning electron microscopy, J. W. Ridge (ERC, Inc.) for the assistance at the flow-tube laboratory, and M. Gusman (ERC, Inc.) for the training on samples' encapsulation. The comments of F. S. Milos (NASA Ames Research Center) and Y.-K. Chen (NASA Ames Research Center) are greatly appreciated.

## References

[1] Chen, Y.-K. and Milos, F. S., "Ablation and Thermal Response Program for Spacecraft Heatshield Analysis," *Journal of Spacecraft and Rockets*, Vol. 36, No. 3, 1999, pp. 475–483.
doi:10.2514/2.3469

[2] Chen, Y.-K. and Milos, F. S., "Two-Dimensional Implicit Thermal Response and Ablation Program for Charring Materials," *Journal of Spacecraft and Rockets*, Vol. 38, No. 4, 2001, pp. 473–481.
doi:10.2514/2.3724

[3] Amar, A. J., Blackwell, B. F., and Edwards, J. R., "One-Dimensional Ablation Using a Full Newton's Method and Finite Control Volume Procedure," *Journal of Thermophysics and Heat Transfer*, Vol. 22, No. 1, 2008, pp. 71–82.
doi:10.2514/1.29610

[4] Amar, A. J., Blackwell, B. F., and Edwards, J. R., "Development and Verification of a One-Dimensional Ablation Code Including Pyrolysis Gas Flow," *Journal of Thermophysics and Heat Transfer*, Vol. 23, No. 1, 2009, pp. 59–71.
doi:10.2514/1.36882

[5] Martin, A. and Boyd, I. D., "Non-Darcian Behavior of Pyrolysis Gas in a Thermal Protection System," *Journal of Thermophysics and Heat Transfer*, Vol. 24, No. 1, 2010, pp. 60–68.
doi:10.2514/1.44103

[6] Chen, Y.-K. and Milos, F. S., "Ablation, Thermal Response, and Chemistry Program for Analysis of Thermal Protection Systems," *Journal of Spacecraft and Rockets*, Vol. 50, No. 1, 2013, pp. 137–149.
doi:10.2514/1.62185

[7] Bose, D., White, T., Santos, J., Feldman, J., Mahzari, M., Olson, M., and Laub, B., "Initial Assessment of Mars Science Laboratory Heatshield Instrumentation and Flight Data," *51$^{th}$ AIAA Aerospace Sciences Meeting including the New Horizons Forum and Aerospace Exposition*, AIAA 2013-0908, Grapevine, TX, 2013.
doi:10.2514/6.2013-908

[8] Mahzari, M., White, T., Braun, R., and Bose, D., "Preliminary Analysis of the Mars Science Laboratory's Entry Aerothermodynamic Environment and Thermal Protection System Performance," *51$^{th}$ AIAA Aerospace Sciences Meeting including the New Horizons Forum and Aerospace Exposition*, AIAA 2013-0185, Grapevine, TX, 2013.
doi:10.2514/6.2013-185

[9] Lachaud, J., Cozmuta, I., and Mansour, N. N., "Multiscale Approach to Ablation Modeling of Phenolic Impregnated Carbon Ablators," *Journal of Spacecraft and Rockets*, Vol. 47, No. 6, 2010, pp. 910–921.
doi:10.2514/1.42681

[10] Lachaud, J. and Mansour, N. N., "Porous-material Analysis Toolbox based on OpenFoam," Accepted for publication on *Journal of Thermophysics and Heat Transfer* on Dec. 4, 2013. In print.

[11] Gokcen, T., Chen, Y.-K., Skokova, K. A., and Milos, F. S., "Computational Analysis of Arc-Jet Stagnation Tests Including Ablation and Shape Change," *Journal of Thermophysics and Heat Transfer*, Vol. 24, No. 4, 2010, pp. 694–707.
doi:10.2514/1.46199

[12] Stackpoole, M., Sepka, S., Cozmuta, I., and Kontinos, D., "Post-Flight Evaluation of Stardust Sample Return Capsule Forebody Heatshield Material," *46$^{th}$ AIAA Aerospace Sciences Meeting and Exhibit*, AIAA 2008-1202, Nevada, NV, 2008.
doi:10.2514/6.2008-1202

[13] Lachaud, J., Mansour, N. N., Ceballos, A., Pejaković, D., L., Z., and Marschall, J., "Validation of a Volume-Averaged Fiber-Scale Model for the Oxidation of a Carbon-Fiber Preform," *42$^{th}$ AIAA Thermophysics Conference*, AIAA 2011-3640, Honolulu, HI, USA, 2011.
doi:10.2514/6.2011-3640

[14] Ellingham, H. J. T., "Reducibility of Oxides and Sulfides in Metallurgical Processes," *Journal of the Society of Chemical Industry*, Vol. 63, No. 5, 1944, pp. 125.
doi:10.1002/jctb.5000630501

[15] Chase, Jr., M. W., "NIST-JANAF Thermochemical Tables (Part I and II)," *Journal of Physical and Chemical Reference Data Monographs*, No. 9 in Monograph, American Institute of Physics, 1998.

[16] McBride, B. J. and Gordon, S., "Computer Program for Calculation of Complex Chemical Equilibrium Compositions and Applications," Reference Publication 1311, NASA, 1996.

[17] Trumble, K. A., Cozmuta, I., Sepka, A. S., Jenniskens, P., and Winter, M., "Postflight Aerothermal Analysis of the Stardust Sample Return Capsule," *Journal of Spacecraft and Rockets*, Vol. 47, No. 5, 2010, pp. 765–774.
doi:10.2514/1.41514

[18] Schindelin, J., Arganda-Carreras, I., Frise, E., Kaynig, V., Longair, M., Pietzsch, T., Preibisch, S., Rueden, C., Saalfeld, S., Schmid, B., Tinevez, J.-Y., White, D. J., Hartenstein, V., Eliceiri, K., Tomancak, P., and Cardona, A., "Fiji: an Open-Source Platform for Biological-Image Analysis," *Nature Methods*, Vol. 9, No. 7, 2012, pp. 676–682.
doi:10.1038/nmeth.2019

[19] Mitchell, M., "Engauge Digitizer - Digitizing Software," http://digitizer.sourceforge.net/.

[20] Helber, B., Chazot, O., Magin, T., and Hubin, A., "Ablation of Carbon Preform in the VKI Plasmatron," *$43^{rd}$ AIAA Thermophysics Conference*, AIAA 2012-2876, New Orleans, LA, USA, 2012.
doi:10.2514/6.2012-2876

[21] Lachaud, J., Bertrand, N., Vignoles, G. L., Bourget, G., Rebillat, F., and Weisbecker, P., "A Theoretical/Experimental Approach to the Intrinsic Oxidation Reactivities of C/C Composites and of their Components," *Carbon*, Vol. 45, 2007, pp. 2768–2776.
doi:10.1016/j.carbon.2007.09.034

[22] Mansour, N. N., Panerai, F., Martin, A., Parkinson, D. Y., MacDowell, A., Haboub, A., Sandstrom, T. A., Fast, T., Vignoles, G. L., and Lachaud, J., "A New Approach To Light-Weight Ablators Analysis: From Micro-Tomography Measurements to Statical Analysis and Modeling," *$44^{th}$ AIAA Thermophysics Conference*, AIAA-2013-2768, San Diego, CA, USA, 2013.
doi:10.2514/6.2013-2768

[23] Marschall, J. and Milos, F. S., "Gas Permeability of Rigid Fibrous Refractory Insulations," *Journal of Thermophysics and Heat Transfer*, Vol. 12, No. 4, 1998, pp. 528–535.
doi:10.2514/2.6372

[24] Mason, E. A. and Malinauskas, A., *Gas Transport in Porous Media: the Dusty-Gas Model*, Chemical Engineering Monograph 17, Elsevier, New York, 1983.

[25] Reid, R. C., Prausnitz, J. M., and Poling, B. E., *The Properties of Gases and Liquids, 4th ed.*, McGraw-Hill, New York, 1987.

[26] Chen, Y.-K. and Milos, F. S., "Navier–Stokes Solutions with Finite Rate Ablation for Planetary Mission

Earth Reentries," *Journal of Spacecraft and Rockets*, Vol. 42, No. 6, 2005, pp. 961–970.
doi:10.2514/1.12248

[27] Park, C., *Nonequilibrium Hypersonic Aerothermodynamics*, John Wiley & Sons, New York, 1990.

[28] Lavigne, O., Dorvaux, J., Drawin, S., and Bacos, M., "Oxidation Model for Carbon-Carbon Composites," *4th International Aerospace Planes Conference, Orlando*, AIAA 1992-210, Orlando, FL, 1992.
doi:10.2514/6.1992-5016

[29] Rosner, D. E. and Allendorf, H. D., "High Temperature Oxidation of Carbon by Atomic Oxygen," *Carbon*, Vol. 6, No. 4, 1965, pp. 153—156.
doi:10.1016/0008-6223(65)90042-4

[30] Rosner, D. E. and Allendorf, H. D., "Comparative Studies of the Attack of Pyrolytic and Isotropic Graphite by Atomic and Molecular Oxygen at High Temperatures," *AIAA Journal*, Vol. 6, No. 4, 1968, pp. 650—654.
doi:10.2514/3.4558

[31] Capitelli, M., Gorse, C., Longo, S., and Giordano, D., "Collision Integrals of High-Temperature Air Species ," *Journal of Thermophysics and Heat Transfer*, Vol. 14, No. 2, 2000, pp. 259–268.
doi:10.2514/2.6517

[32] Zhang, L., Pejaković, D. A., Geng, B., and Marschall, J., "Surface Modification of Highly Oriented Pyrolytic Graphite by Reaction with Atomic Nitrogen at High Temperatures," *Applied Surface Science*, Vol. 257, No. 13, 2011, pp. 5647–5656.
doi:http://dx.doi.org/10.1016/j.apsusc.2011.01.066

[33] Zhang, L., Pejaković, D. A., Marschall, J., and Fletcher, M. D. D. G., "Laboratory Investigation of the Active Nitridation of Graphite by Atomic Nitrogen," *Journal of Thermophysics and Heat Transfer*, Vol. 26, No. 1, 2012, pp. 10–21.
doi:10.2514/1.56781

[34] Poovathingal, S., Schwartzentruber, T. E., Srinivasan, S. G., and van Duin, A. C. T., "Large Scale Computational Chemistry Modeling of the Oxidation of Highly Oriented Pyrolytic Graphite," *The Journal of Physical Chemistry A*, Vol. 117, No. 13, 2013, pp. 2692–2703.
doi:10.1021/jp3125999

[35] Hahn, J., "Kinetic Study of Graphite Oxidation along Two Lattice Directions," *Carbon*, Vol. 43, No. 7, 2005, pp. 1506 – 1511.
doi:http://dx.doi.org/10.1016/j.carbon.2005.01.032

[36] Hahn, J. R. and Kang, H., "Vacancy and Interstitial Defects at Graphite Surfaces: Scanning Tunneling

Microscopic Study of the Structure, Electronic Property, and Yield for Ion-induced Defect Creation," *Physical Review B*, Vol. 60, 1999, pp. 6007–6017.
doi:10.1103/PhysRevB.60.6007

[37] Lee, K. H., Lee, H. M., Eun, H. M., Lee, W. R., Kim, S., and Kim, D., "The Electronic Structure of Lattice Vacancies on the STM Image of a Graphite Surface," *Surface Science*, Vol. 321, No. 3, 1994, pp. 267 – 275.
doi:http://dx.doi.org/10.1016/0039-6028(94)90192-9

[38] Vignoles, G. L., Lachaud, J., Aspa, Y., and Goyhénèche, J.-M., "Ablation of Carbon-based Materials: Multiscale Roughness Modelling," *Composites Science and Technology*, Vol. 69, 2009, pp. 1470–1477.
doi:10.1016/j.carbon.2007.09.034